

# Potassium dependent structural changes in the selectivity filter of HERG potassium channels

Received: 5 December 2023

Accepted: 25 July 2024

Published online: 29 August 2024

 Check for updates

Carus H. Y. Lau <sup>1,2,7</sup>, Emelie Flood <sup>3,7</sup>, Mark J. Hunter<sup>1,2,7</sup>, Billy J. Williams-Noonan<sup>3</sup>, Karen M. Corbett <sup>3</sup>, Chai-Ann Ng <sup>1,2</sup>, James C. Bouwer <sup>4</sup>, Alastair G. Stewart <sup>2,5</sup>, Eduardo Perozo<sup>6</sup>, Toby W. Allen <sup>3</sup> ✉ & Jamie I. Vandenberg <sup>1,2</sup> ✉

The fine tuning of biological electrical signaling is mediated by variations in the rates of opening and closing of gates that control ion flux through different ion channels. Human ether-a-go-go related gene (HERG) potassium channels have uniquely rapid inactivation kinetics which are critical to the role they play in regulating cardiac electrical activity. Here, we exploit the K<sup>+</sup> sensitivity of HERG inactivation to determine structures of both a conductive and non-conductive selectivity filter structure of HERG. The conductive state has a canonical cylindrical shaped selectivity filter. The non-conductive state is characterized by flipping of the selectivity filter valine backbone carbonyls to point away from the central axis. The side chain of S620 on the pore helix plays a central role in this process, by coordinating distinct sets of interactions in the conductive, non-conductive, and transition states. Our model represents a distinct mechanism by which ion channels fine tune their activity and could explain the uniquely rapid inactivation kinetics of HERG.

Ion channels may exist in one of three main conformational states: closed, open, or inactivated. Inactivation describes the process whereby ion channels enter a non-conducting state in the presence of a prolonged activating stimulus. Differences in rates of inactivation of ion channels are a major determinant of their specific physiological functions<sup>1</sup>. In HERG K<sup>+</sup> channels, the combination of the rapidity, voltage dependence, and K<sup>+</sup> sensitivity of inactivation is critical for regulating cardiac repolarization and the response to ectopic beats<sup>2–4</sup>. Furthermore, both hypokalaemia<sup>5</sup> and mutations that affect inactivation gating<sup>6,7</sup> increase the risk of cardiac arrhythmias. Despite the clinical importance of HERG potassium channels, we still do not understand the structural basis for how they inactivate.

One of the major mechanisms underlying inactivation in K<sup>+</sup> channels is conformational changes in the selectivity filter resulting in loss of conduction<sup>1</sup>. There is high sequence homology in the selectivity filter of different classes of potassium channels<sup>1</sup> with subtle sequence differences in the selectivity filter and immediately behind the filter contributing to the differences in the rates of inactivation of different K<sup>+</sup> channels<sup>8,9</sup>. For example, the rate of HERG K<sup>+</sup> channel inactivation is approximately two orders of magnitude faster than inactivation of the bacterial KcsA K<sup>+</sup> channel and approximately three orders of magnitude faster than c-type inactivation of the eukaryotic Shaker K<sup>+</sup> channel<sup>4</sup>. Why inactivation in HERG is so fast remains unresolved.

<sup>1</sup>Mark Cowley Lidwill Research Program, Victor Chang Cardiac Research Institute, Darlinghurst, NSW, Australia. <sup>2</sup>School of Clinical Medicine, UNSW Sydney, Sydney, NSW, Australia. <sup>3</sup>School of Science, RMIT University, Melbourne, VIC, Australia. <sup>4</sup>Molecular Horizons and School of Chemistry and Molecular Bioscience, and ARC Centre for Cryoelectron Microscopy of Membrane Proteins, University of Wollongong, Wollongong, NSW, Australia. <sup>5</sup>Computational and Structural Biology Division, Victor Chang Cardiac Research Institute, Darlinghurst, NSW, Australia. <sup>6</sup>Department of Biochemistry and Molecular Biology, The University of Chicago, Chicago, IL, USA. <sup>7</sup>These authors contributed equally: Carus H. Y. Lau, Emelie Flood, Mark J. Hunter. ✉e-mail: [toby.allen@rmit.edu.au](mailto:toby.allen@rmit.edu.au); [j.vandenberg@victorchang.edu.au](mailto:j.vandenberg@victorchang.edu.au)

One approach that has been used to probe the structural basis of  $K^+$  channel selectivity filter gating is to determine structures in the presence of different  $K^+$  concentrations<sup>10–12</sup>. In the bacterial KcsA  $K^+$  channel, the most extensively studied  $K^+$  channel structure, the selectivity filter has a cylindrical shape in the presence of 300 mM  $K^+$  with five  $K^+$  ion binding sites, denoted S0–S4<sup>10,13</sup>. In the presence of 3 mM  $K^+$ , the KcsA selectivity filter has a constriction at the level of G77  $\text{C}\alpha$ <sup>10,11</sup> and rotation of the valine (V76) backbone carbonyls to point  $-90^\circ$  away from the central axis<sup>10</sup>. These changes are also observed in mutant channels with a forced open activation gate<sup>14</sup> and recapitulated in MD simulations<sup>11,15–17</sup>. Thus, a consensus has emerged that the inactivated state of KcsA has an hourglass shaped selectivity filter with the constriction at the level of G77. In contrast to KcsA, a recent study of heterodimeric  $K_{2P,1}$  channels showed that  $<1$  mM  $K^+$  causes an asymmetrical constriction and dilatation of the filter<sup>12</sup>. Furthermore, in the Shaker family of voltage-gated  $K^+$  channels, mutations that enhance inactivation result in dilatation of the extracellular half of the filter with no constriction at the central glycine<sup>18–21</sup>. Thus, while the structures of the selectivity filter in the conductive state of different classes of potassium channels are similar, it is likely that they have adopted different mechanisms for conversion to a non-conducting state.

Cryo-EM studies of WT HERG and the inactivation-deficient S631A HERG channels, in the presence of 300 mM  $K^+$ , revealed an  $-10^\circ$  rotation of F627, the phenylalanine in the selectivity filter<sup>22</sup>. The authors suggested that such a subtle structural change was consistent with the rapidity of inactivation in HERG<sup>22</sup>. Conversely, Molecular dynamics (MD) simulation studies of the WT HERG structure suggested that the transition from conducting to non-conducting selectivity filter structures could involve asymmetric buckling of the selectivity filter<sup>23,24</sup>, and/or dilation of the upper filter<sup>23,25</sup>. An alternative explanation for the similarity of the WT and S631A HERG structures is that they both represent subtly different conductive state structures<sup>23,26,27</sup>. Thus, the structural basis for HERG inactivation remains unresolved.

Here, to explore the structural basis for the rapidity of HERG inactivation, we use cryo-EM to investigate the potassium dependent structural changes in the selectivity filter and molecular dynamics (MD) simulations to explore how  $K^+$  dependent rearrangements of the selectivity filter can occur so rapidly.

## Results

### Structures of HERG in high- $K^+$ and low- $K^+$ conditions

To interrogate the potassium dependence of the hERG channel structure we purified a WT hERG construct, with the predicted unstructured regions spanning residues 140–380 and 870–1006 deleted<sup>22</sup>, in buffers containing either 300 mM KCl (high-K) or 3 mM KCl (low-K). Structures were solved using RELION; a flow chart summarizing the EM data processing is shown in Supplementary Fig. S1. Structures were initially solved with C1 symmetry, however, as there was no substantial asymmetry between subunits (Supplementary Fig. S2), we solved the structures using C4 symmetry to improve the overall resolution (Fig. 1A) and the C4 maps were used for all subsequent analyses. The global resolution was 3.3 Å for high- $K^+$  and 3.0 Å for low- $K^+$  (Fig. 1B, Supplementary Fig. S1, S2, Supplementary Table S1). The local resolution was highest in the vicinity of the selectivity filter region in both the high-K and low-K structures (Fig. 1B).

The density maps for low-K and high-K structures are very similar, with the major differences occurring in the selectivity filter region (Fig. 1C). The most obvious density difference corresponds to the side chain and backbone of F627 with other notable differences in the vicinity of the backbone of G626, side chain and backbone of V625, side chain of S620, and side chain of Y616 (Fig. 1C). There are also differences in the density along the ion conduction pathway, which are discussed in more detail below.

The root mean square deviation (RMSD) for the backbone atoms of the best fit structures for the low-K and high-K maps, aligned on the

pore helix, is 1.2 Å in the selectivity filter compared to 0.3 Å in the pore domain helices: S5, S5P, and S6; consistent with the minimal difference in density seen away from the selectivity filter (Supplementary Fig. S3). In the high-K structure, the selectivity filter backbone carbonyls for S624, V625, G626, and F627 point towards the central axis (Fig. 1D), as seen in previously reported structures for WT HERG<sup>22,28</sup>, and shows a cylindrical profile (Fig. 1E) similar to that seen in KcsA, Trek-1, and Shaker, when determined in the presence of high- $K^+$ <sup>10,12,18</sup>.

The differences seen in the low-K structure relative to the high-K structure include (i) a lateral displacement of the F627 backbone atoms and side chain (ii) displacement of the G626 backbone carbonyls towards the central axis, (iii) rotation of the V625 backbone carbonyls such that they now point away from the central axis (bidirectional arrowhead, Fig. 1D) causing the G626 backbone amide to point towards the central axis (arrowhead in Fig. 1D), and (iv) a small lateral displacement of the S624 side chain. At the resolution of our structures, we cannot see the precise location of backbone carbonyls. Nevertheless, we can infer that in the low-K structure the V625 backbone carbonyls are flipped to face away from the central cavity, based on (i) higher probability in the Ramachandran plot (Supplementary Fig. S4) and (ii) molecular dynamics flexible fitting (MDFF) simulations to the cryo-EM density maps (Supplementary Fig. S5). As a result of the V625 backbone carbonyls flipping there is a dilation of the ion conduction pathway in the vicinity of V625 in the low-K HERG structure (Fig. 1E) which is quite distinct to the hourglass profile seen in KcsA low-K (Supplementary Fig. S6).

In previous MD simulations, it has been shown that the high-K HERG structure can conduct  $K^+$  ions<sup>23</sup>. To specifically investigate how V625 backbone carbonyls pointing inwards, versus outwards, affect ion conduction, we undertook simulations of the high-K and low-K structures in the presence of high ion concentration (500 mM) and high inward-driving membrane potential ( $-500$  mV). To trap each structure in the cryo-EM conformation without strongly affecting filter dynamics, weak flat-bottom restraints on S620 H-bonds to the V625-G626 and G626-F627 linkages were applied (not acting unless the conformation attempts to change; see “Methods”). The filter is seen to conduct ions with the V625 backbone carbonyls pointing inwards (Fig. 1F; two independent 500 ns simulations shown in Supplementary Fig. S7). Furthermore, all but one of the seven conduction events observed (Supplementary Fig. S7c) showed a soft knock-on mechanism, i.e., there was a water molecule separating adjacent  $K^+$  ions during the translocation of ions between S1-S2-S3-S4  $K^+$  ion binding sites. As expected, the filter cannot conduct ions when the V625 backbone carbonyls point outwards (Fig. 1F; two independent 500 ns simulations shown in Supplementary Fig. S7).

In summary, our data, as well as the previous studies of HERG, show a cylindrical-shaped selectivity filter in the presence of 300 mM  $K^+$ . Conversely, in the presence of 3 mM  $K^+$ , the selectivity filter has a non-canonical shape with flipped V625 backbone carbonyls and is not able to conduct  $K^+$  ions.

### Different Hydrogen bond networks stabilize low-K and high-K structures of HERG

There are multiple residues in the vicinity of the selectivity filter that are either unique to HERG (e.g. S620) or conserved only in the *ether-a-go-go* subfamily of voltage-gated potassium channels (e.g., Y616, F617, F627, N629; Fig. 2A). Our structures reveal a series of hydrogen bond networks (centered on S620) and hydrophobic interactions (involving F627 and F617) that contribute to stabilization of the high-K and/or low-K structures. A first set of interactions are present in both the high-K and low-K structures: (i) the S620 backbone carbonyl interacts with the backbone amide of V625 to anchor the bottom of the filter; (ii) the Y616 side chain hydroxyl and backbone amide of N629 anchor the top of the filter to the pore helix (green dashed lines in Fig. 2B) and (iii) an intersubunit hydrophobic interaction between the side chains of F627

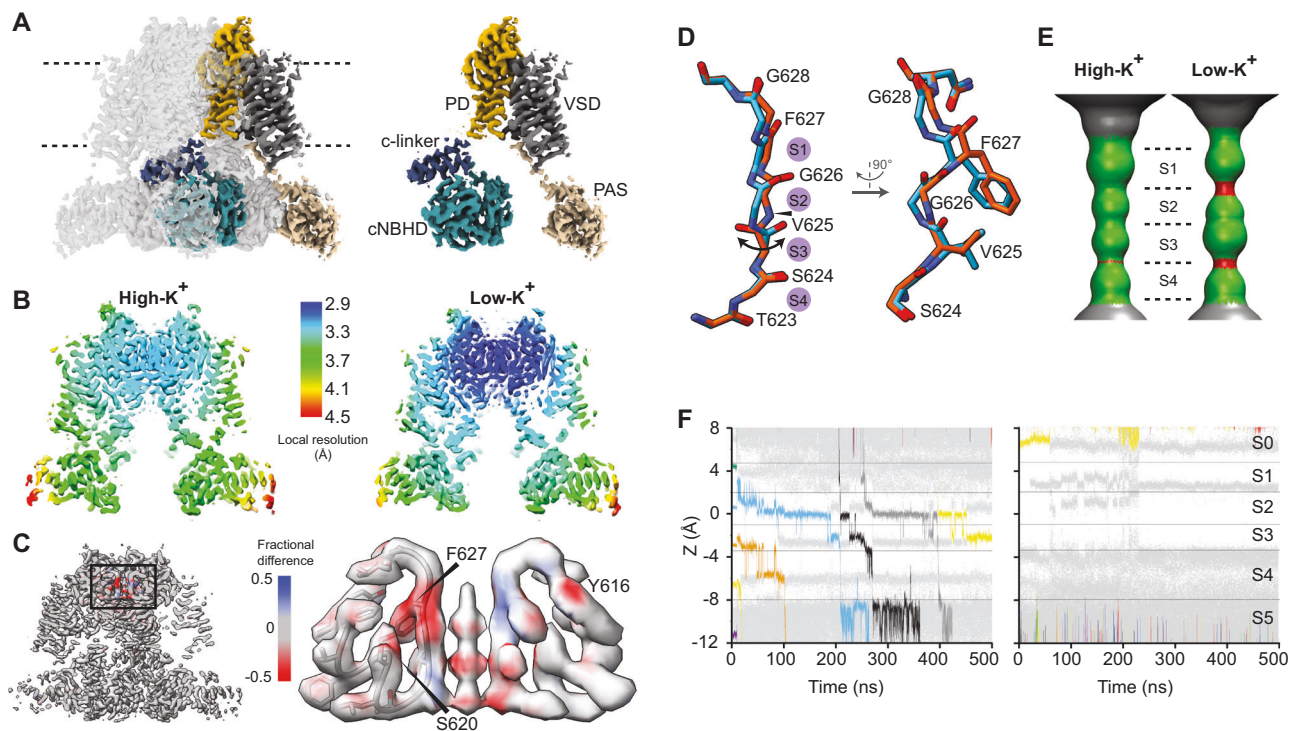


**Fig. 1 | Cryo-EM structure of WT-HERG solved in presence of high-K and low-K.**

**A** Cryo-EM map of low-K WT-HERG (contour 6 $\sigma$ ) with a single subunit of the channel highlighted to illustrate the major domains: pore-domain (PD), voltage sensor domain (VSD), cyclic nucleotide binding homology domain (cNBHD), per-arnt-sim (PAS) domain. **B** Local resolution of cryo-EM maps solved using C4 symmetry. The resolution range of the transmembrane regions are reported in Supplementary Table 1. **C** Fractional difference map for high-K and low-K maps. Maps were normalized and low pass filtered to 3.3 Å before fractional difference was calculated using TEMpy:Difference Map tool in CCPEM<sup>53</sup>. Red indicates density only present in the low-K map (density missing in high-K) and blue represents density only present in the high-K map; thresholding 0.0252 (8 $\sigma$ ). Right panel shows a close-up view of the selectivity filter (high-K, blue and low-K, red). In addition to the selectivity filter residues, there are differences seen for the S620 and Y616 side chains. **D** overlay of low-K (orange) and high-K selectivity filter structures,

aligned to the pore helix. In the left panel the lateral and upward displacement of the the F627/G628 backbone in the low-K structure is apparent as is a small lateral displacement of the S624 side chain. On the rotated view, the central displacement of the G626 backbone carbonyl, flipping of the V625 backbone carbonyl (bidirectional arrows) and resulting central facing G626 amide (arrowhead) are apparent in the low-K structure. **E** The high-K structure has a canonical selectivity filter HOLE profile, whereas the low-K structure shows dilation in the vicinity of V625 and constrictions at the level of S624 and G626. This is distinct to the single constriction observed in the KcsA low-K filter at G77 (equivalent to G626, see Supplementary Fig. S6). **F** Example MD simulations showing ion conduction events when the V625 backbone carbonyls point towards the central cavity (to mimic high-K structure), but no conduction is seen when the V625 backbone carbonyls point outwards (to mimic low-K structure). Ions are shown as colored lines, water molecules as gray points.

and F617 cradles the central region of the selectivity filter (Fig. 2C). Together, these interactions form a scaffold that helps to stabilize the structure of the selectivity filter.

Second, the side chain of S620 coordinates distinct sets of interactions in the high-K and low-K structures. In the high-K structure, the S620 side chain interacts with the backbone amides of F627 and G626, while in the low-K structure, the S620 side chain interacts with the flipped V625 backbone carbonyl (Fig. 2B). Notably, mutations to V625 and F627 enhance inactivation when introduced into the WT HERG background, but no longer do so when introduced into the S620T background (Fig. 2D). S620T has a dominant effect on inactivation which indicates that the two mutants are not affecting inactivation via independent mechanisms consistent with V625 and F627 interacting with S620. It is not obvious how side chain mutations to V625 and F627 affect inactivation as they will not directly affect the backbone carbonyls that are critical for coordinating K<sup>+</sup> ions. Given the tight packing in the local environment, it is plausible that conservative side chain modifications are sufficient to alter the local environment but not to such a degree that it overcomes the effect of the S620T mutation to stabilize the conducting conformation.

S620 was first identified as a critical residue for HERG inactivation 25 years ago<sup>8,9</sup>. Here, we have identified how S620 side chain contributes to inactivation gating. Specifically, the S620 side chain alternatively stabilizes the canonical selectivity filter structure seen in high-

K structure through interactions with the amide backbone of G626 and F627 (Fig. 2B), and then stabilizes the flipped V625 backbone carbonyl in the non-canonical selectivity filter structure seen in low-K structure (Fig. 2B).

### Effect of K<sup>+</sup> ions on selectivity filter structure

There are differences in the density along the ion conduction pathway between the high-K and low-K structures which can be seen in both C1 (see supplementary Fig. S2) as well as C4 maps (Fig. 3A). To explore how changes in K<sup>+</sup> ion occupancy could affect selectivity filter structure we turned to molecular dynamics (MD) simulations. First, WT channels were embedded in palmitoylcholine-phosphatidylcholine lipid bilayers with 1, 2, or 3 ions constrained in the five K<sup>+</sup> ion binding sites (denoted S0, S1, S2, S3, S4), allowing sampling of the different conformations of the filter (Supplementary Fig. S8). For simulations with single or multiple ions present, the backbone carbonyls for the respective ion binding sites tended to point inwards (see Supplementary Fig. S8). The exception was V625, which contributes to coordination of K<sup>+</sup> ions in S2 or S3 sites, where some fraction of the backbone carbonyls were observed to be directed away from the central axis. For example, for S0/S2/S4 occupancy, at least one of the four V625 backbone carbonyls flips out 84 ± 6% of the time (Fig. 3B). There were no single or multiple ion occupancies that include a K<sup>+</sup> ion in S2 or S3 where all four V625 backbone carbonyls pointed towards

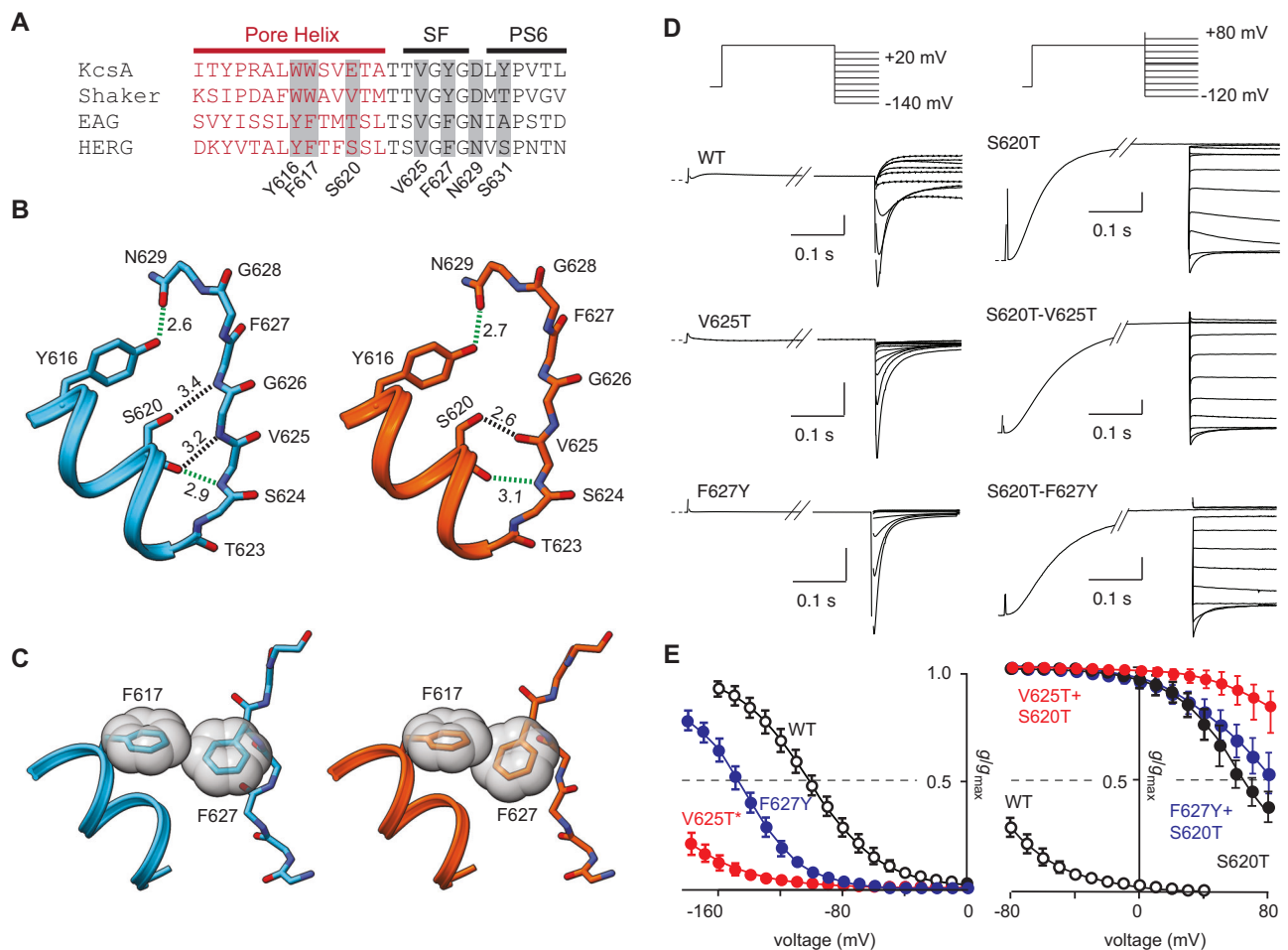


**Fig. 2 | Different hydrogen bond networks stabilize conducting and non-conducting selectivity filters.** **A** Sequence alignment of the pore-helix, selectivity filter and PS6 linker region; residues unique to HERG or present only in the EAG subfamily are highlighted. **B** Hydrogen bond networks seen in high-K (blue) and low-K (orange) structures. Interactions conserved in both structures (Y616-side chain hydroxyl to N629-side chain oxygen and S620 backbone carbonyl to V625 backbone amide) are shown in green dashed lines. The S620 side chain hydroxyl interacts with the G626/F627 backbone amides in the high-K structure but with the flipped V625 backbone carbonyl in the low-K structure. **C** Intersubunit hydrophobic interactions between the tips of the side chains of F627 and F617, seen in both high-K (blue) and low-K (orange) structures. **D** Exemplar families of current traces recorded from V625T and F627Y in WT and S620T backgrounds. Vertical scale bar

is 500 nA in each panel. WT, V625T, and F627Y channels pass little current during the initial +40 mV step, as channels are inactivated. Conversely, in S620T, S620T-V625T, and S620T-F627Y channels there is a large current at +40 mV and these channels only start to inactivate at more positive potentials. Note the different range of voltages used for tail current recordings for S620T channels. **E** Boltzmann fits to steady-state inactivation curves for mutants shown in panel **(D)**. Mutations to V625 and F627 promote inactivation in the WT HERG channels. Conversely, in the presence of S620T, which reduces inactivation, neither V625T nor F627Y enhance inactivation. This is consistent with interactions between S620T-V625T and S620T-F627Y affecting the transition between the conducting and non-conducting states of HERG (WT,  $n = 16$ ; V625,  $n = 9$ ; F627Y,  $n = 10$ ; S620T,  $n = 10$ ; V625T-S620T,  $n = 8$ ; F627Y-S620T,  $n = 12$ ).

the axis of symmetry more than 50% of the time. This contrasts with other  $K^+$  channels where a  $K^+$  ion held in S2 (or S0/S2/S4 or S1/S3) is sufficient to stabilize the selectivity filter valine backbone carbonyls pointing inwards<sup>15,29</sup>. A second notable feature is that the G628 backbone carbonyls do not point inwards for any ion configuration (Fig. 3B, Supplementary Fig. S8) and when ions are not held in S0 or S1, there is a propensity for the F627 backbone carbonyls to rotate away from the central axis. We also note during the simulations of ion conduction (Fig. 1F, Supplementary Fig. S7) that there was a tendency for F627 backbone carbonyls to rotate away from the pore when ions were not present in S0/S1. These data are consistent with observations from electrophysiology experiments that  $K^+$  exit from the upper end of the filter represents the first step in the transition from the open to inactivated states of HERG<sup>30</sup>. Lastly, when there are no ions in the filter then the backbone carbonyls for all residues, apart from S624, are highly dynamic (Supplementary Fig. S8).

The simulations so far suggest an important role for rotation of the V625 backbone carbonyls. To directly probe the energetics of this

transition, we used umbrella sampling simulations to map out the free energy of rotation of the V625-G626 peptide linkage. With ions present in the canonical conducting configuration, S0/S2/S4 or S1/S3, there are two minima in the umbrella sampling: at  $\Psi \sim -50^\circ$  (V625 carbonyl non-flipped) and  $\Psi \sim 70^\circ$  (flipped V625 carbonyl, Fig. 3C). The free energy difference between flipped and non-flipped V625 backbone carbonyls is  $<1 \text{ kcal mol}^{-1}$  for the S0/S2/S4 configuration and  $-2 \text{ kcal mol}^{-1}$  for S1/S3 configuration; which may be compared to a published estimate of  $-9 \text{ kcal mol}^{-1}$  for KcsA<sup>15</sup>. Also, there is only a 4–5  $\text{kcal mol}^{-1}$  barrier (at  $\Psi \sim 35^\circ$ ) separating the flipped and non-flipped V625 backbone carbonyl conformations in HERG, compared to  $-12 \text{ kcal mol}^{-1}$  for KcsA<sup>15</sup>. Thus, rotation of HERG V625 backbone carbonyls (both from flipped to non-flipped and vice versa) is energetically possible, when  $K^+$  ions are present in the filter, and can occur rapidly due to the low energy barrier for flipping.

All the above simulations relied on having ions constrained in specific binding sites in the filter. To investigate the distribution of unconstrained  $K^+$  ions in the HERG selectivity filter, and achieve a more

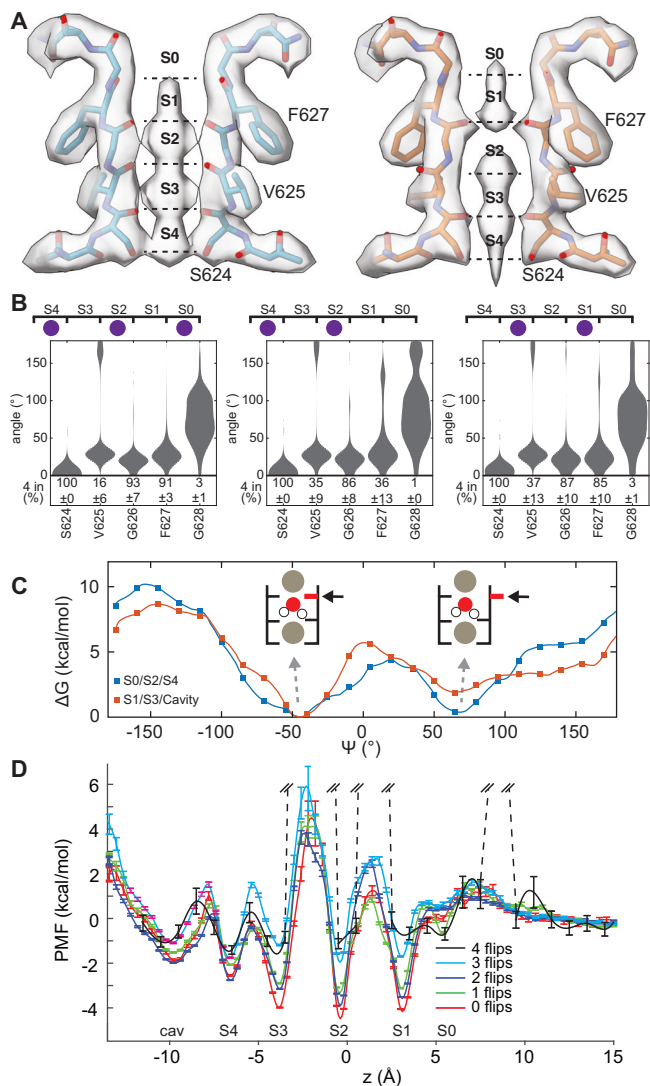


**Fig. 3 | V625 backbone carbonyls can flip when K<sup>+</sup> ions are present in the filter.**

**A** Structures of high-K (left) and low-K (right) selectivity filters determined with C4 symmetry. The labels S0–S4 highlight canonical K<sup>+</sup> ion binding sites.

**B** Distribution of backbone carbonyl angles,  $\theta$  ( $0^\circ$  indicates pointing towards center of the pore) from MD simulations with ions held in the configurations shown. The proportion of time all 4 backbone carbonyls were pointing inwards (defined as  $<70^\circ$  deviation from  $0^\circ$ ) is shown at the bottom. Backbone carbonyl angle distributions for single ion configurations are shown in Supplementary Fig. S8. **C** Free energy profile derived from Umbrella Sampling of rotation of the  $\Psi$  angle of the V625-Gly626 linkage when ions are held in S0/S2/S4 (blue), or S1/S3/Cav (cavity) (orange). The energy minima for V625 backbone carbonyls pointing towards and away from the central axis are indicated at  $\Psi = -50^\circ$  and  $+70^\circ$ , respectively.

**D** Potential mean force for ion binding in the filter from REST2 simulations for 0 (red), 1 (green), 2 (blue), 3 (cyan), or 4 (black) flipped V625 backbone carbonyls. Barriers for the 4 flipped conformation that are not well sampled are shown as black dashed lines. Data shown as mean  $\pm$  SD obtained from MBAR<sup>33</sup>.

unbiased sampling of possible selectivity filter conformations, we used replica exchange with solute tempering (REST2) simulations<sup>31</sup>; totaling 16  $\mu$ s of enhanced-sampling simulation time. There were frequent movements of ions between sites, and in addition to the canonical configurations we also observed ions present in S2 and S3 simultaneously, further attracting backbone carbonyl groups towards the central axis (Supplementary Fig. 9C). However, given evidence for the effect of force field on propensity for channel closure<sup>32</sup>, the distribution of ion configurations and their effects on filter structure may differ in other models.

We next analyzed the free energy profile of ion distribution in the filter according to the number of flipped V625 backbone carbonyls (Fig. 3D). Using Multistate Bennett Acceptance Ratio (MBAR)<sup>33</sup>, we exploit the sampling in all 16 REST2 replicas to obtain an optimal estimate of free energies in the unscaled replica. We achieve good sampling of wells and barriers for 0–3 flips, but only capture the low free energy regions with 4 flips. The free energy wells for S1, S2, and S3 are 3–4 kcal/mol when 0, 1, or 2 V625 backbone carbonyls are flipped, but become significantly destabilized when 3 or 4 V625 backbone carbonyls are flipped. This suggests that 0, 1, or 2 flipped V625 backbone carbonyls are consistent with a conductive conformation while 3 or 4 flipped V625 backbone carbonyls may relate to the non-conducting form of the channel.

### The transition state between flipped and non-flipped V625 backbone carbonyls

When we amalgamated the constrained ion MD simulations and clustered frames based on the backbone angles of the selectivity filter residues in individual subunits (Supplementary Fig. S10), there were two major clusters: Cluster 1 (41% of frames) has backbone carbonyls of S624, V625, G626, and F627 pointing inwards (Fig. 4A: blue, Supplementary Fig. S10) and Cluster 2 (30% of frames) has the V625 backbone carbonyls flipped to point outwards (Fig. 4A: orange, Supplementary Fig. S10). In addition to the expected interactions between the S620 side chain and F627/G626 peptide amides (Cluster 1) and with the flipped V625 backbone carbonyl (cluster 2) we observed that the S620 side chain spends  $\sim 5\%$  (cluster 1) or  $\sim 25\%$  (cluster 2) of the time interacting with the Y616 backbone carbonyl oxygen (Fig. 4B). When the S620 side chain is interacting with the Y616 backbone carbonyl oxygen, the V625-G626 peptide linkage would be free to rotate, thereby facilitating the transition between the conducting and non-conducting states. To explore this hypothesis, we next analyzed 2D free energy surfaces for S620 side chain interactions with selectivity filter residues and Y616 as a function of the angle of rotation of the V625 backbone carbonyl in the REST2 simulations with MBAR, which allows more complete sampling of all states (Fig. 4C–F). The four interactions that the S620 side chain can participate in, occupy wells in the 2D free energy surfaces that are labeled (i) F627/G626 amides when the V625 backbone carbonyls point inwards, (ii) Y616 backbone carbonyl when the V625 backbone carbonyls point outwards and (iii) Y616 backbone carbonyl when the V625 backbone carbonyl point inwards in Fig. 4C–F. When S620 is interacting with the Y616 backbone, the free energy barrier for valine flipping is only  $1.8 \pm 0.1$  kcal mol<sup>-1</sup>, whereas the transition is otherwise forbidden (Fig. 4F). Thus, the S620 side chain-Y616 backbone interaction acts like a catalyst to lower the free energy barrier of the transition state and enable rapid rotation of the V625 backbone carbonyl oxygen. When the V625 backbone carbonyl is flipped, the free energy barrier for S620 side chain to switch between interacting with the Y616 backbone carbonyl and the V625 backbone carbonyl is  $5.9 \pm 0.5$  kcal/mol. We suggest that the V625 backbone carbonyl can rotate back and forth frequently but it needs to be trapped in the flipped state by an interaction with the S620 side chain to stabilize the non-conducting conformation.

### Comparison between WT and S631A HERG

In addition to a structure of WT HERG, Wang and Mackinnon determined the structure of the S631A mutant, which stabilizes occupancy of the open state at 0 mV<sup>34</sup>. In Fig. 5, we show the selectivity filters of our low-K and high-K WT structures and compare to the previously determined high-K S631A structure (PDB: 5VA3). The three structures have been aligned based on the pore helix region. In addition to rotation of the F627 residue between S631A and WT high-K (as noted previously<sup>22</sup>) the WT HERG filter is displaced upwards relative to the

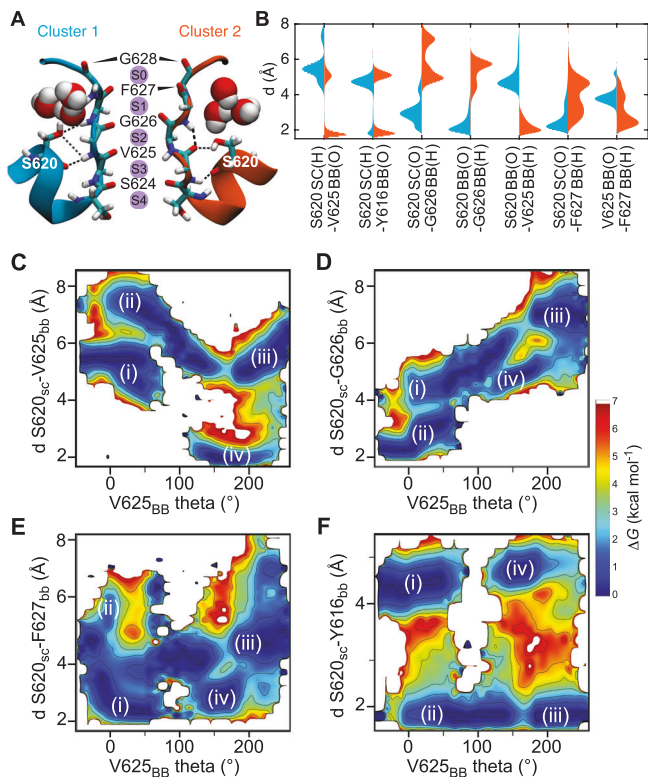


**Fig. 4 | A low energy barrier separates conducting and non-conducting states of the HERG selectivity filters. A** Representative structures of the two major clusters observed in constrained ion MD simulations. In Cluster 1 (blue, 41%) all selectivity filter backbone carbonyls point centrally. Cluster 2 (orange, 30%) has a flipped V625 backbone carbonyl that interacts with S620. **B** summary of distances between the indicated residue pairs for cluster 1 (blue) and cluster 2 (orange). Note that the S620 side chain is located  $-2$  Å from the Y616 backbone carbonyl  $-5\%$  of the time in cluster 1 and  $-25\%$  of the time in cluster 2. **C–F** Two-dimensional free energy surfaces obtained from REST2 simulations with MBAR for S620 side chain interactions with **(C)** V625 backbone carbonyl, **(D)** G626 backbone amide, **(E)** F627 backbone amide, and **(F)** Y616 backbone carbonyl, plotted as a function of rotation of the V625 backbone carbonyl angle ( $\theta$ ). Low free energy states are indicated for S620 interacting with (i) F627/G626, (ii) S620 interacting with Y616 backbone carbonyl when V625 backbone carbonyl points inwards, (iii) S620 interacting with Y616 backbone when V625 backbone carbonyl points outwards, and (iv) S620 interacting with flipped V625 backbone carbonyl. Qualitatively similar 2D PMF plots were obtained when we analyzed the amalgamated constrained ion simulations (see Supplementary Fig. S11).

filter in S631A. The higher displacement of the WT HERG filter raises the level of the V625 backbone carbonyls to be closer to the level of S620 side chain. Thus, we suggest that the higher filter in the WT high-K structure is better placed to allow rotation about the V625-G626 peptide linkage and stabilization of the flipped V625 backbone carbonyl by interacting with the S620 side chain and so can be considered primed to adopt a non-conducting structure as soon as  $K^+$  ions leave the filter. Conversely, we suggest that in the S631A channel, the lower filter would promote interaction between S620 and the amide backbones of G626 and F627 to stabilize the conductive filter. This model needs to be tested by investigating how mutations to residues that are known to affect inactivation gating, both within the filter region as well as in the pore helix, PS6 domain and the extracellular turret region affect the structure of the selectivity filter.

## Discussion

From the cryo-EM and MD studies, we propose a model for the  $K^+$ -dependent transition between conducting and non-conducting states of HERG that is summarized in Fig. 6. The conducting state is

characterized by the S620 side chain interacting with the amide backbones of F627 and G626 (Fig. 6A). Transition from conducting to non-conducting is initiated by  $K^+$  ions leaving the upper filter (Fig. 6B). The transition state (Fig. 6C, D) is characterized by the S620 side chain interacting with the Y616 backbone, which leaves the Val-Gly peptide bond free to rotate. The non-conducting state is stabilized by the flipped V625 backbone carbonyl binding to the S620 side chain, and it is likely that at least three, and possibly all four, V625 backbone carbonyls need to be maintained in the flipped state for the channel to become non-conductive (Fig. 3D). The high barrier between S2 and S3, which impedes ions moving upwards, means that ions may leave and not be replenished quickly, leaving the upper filter free of ions for a period, which facilitates transition to a non-conducting state. Importantly, our model explains the critical role for S620<sup>8,9</sup>, which is validated by the observation that this residue is unique to HERG and that the homologous HEAG channels, where the corresponding residue is a threonine, do not inactivate<sup>8</sup>. Our model is also supported by an extensive literature showing that mutations to the residues involved in the interactions described above (Y616, S620, V625, G626, F627) affect inactivation gating in HERG<sup>8,24,35–38</sup>.

Based on crystallography studies of KcsA in high (150–300 mM) and low (3 mM) potassium, inactivation was proposed to involve constriction of the central glycine residue<sup>10,14</sup>, rotation of V76 backbone carbonyls away from the central axis<sup>10,11,17,39,40</sup>, rearrangement of water-mediated hydrogen bond networks, and decrease in the number of water molecules behind the selectivity filter<sup>11,14,17</sup>. In HERG, there is more rotation of the V625 backbone carbonyls but a less prominent constriction at the level of G626 (for both the backbone carbonyls and backbone C $\alpha$ ), compared to KcsA (Fig. 7). The interaction between the flipped V625 backbone carbonyls and the S620 side chain hydroxyl in HERG likely contributes to stabilizing the “non-conducting” conformation of HERG. Thus, HERG may adopt two modes with V625 backbone carbonyls flipping back and forth (while the S620 side chain is bound to the Y616 backbone carbonyl oxygen) and a longer-lived flipped state when the flipped V625 backbone carbonyl oxygen interacts with the S620 side chain. Conversely, in KcsA rapid flipping of the V76 backbone carbonyls is associated with a flickering state<sup>40,41</sup> whereas in the inactivated state there is an increase in water behind the filter with the four V76 backbone carbonyls rotated  $-90^\circ$  away from the central axis where they form a ring-like water-mediated hydrogen bonding network that stabilizes the constricted structure<sup>16</sup>. A similar mechanism has also been observed in MthK channels<sup>29</sup>. It is not possible to observe water molecules at the resolution of our cryo-EM structures, but our MD simulations suggest that there is only a modest rearrangement with no net change in the number of water molecules behind the filter during the transition between conducting and non-conducting states (Supplementary Fig. 12), albeit with the appearance of a free energy minimum that demonstrates a water molecule is driven down towards the flipped V625 upon change to the non-conducting state. The no net change in water molecules may also contribute to kinetics of HERG inactivation being faster than that observed for KcsA where the rate of inactivation is determined by the diffusion limited rate of water binding<sup>17</sup>.

S620 in HERG is equivalent to E71 in KcsA and both play critical roles in inactivation, albeit in different ways that reflect the distinctive physiochemical properties of the respective side chains. In two previous MD studies of HERG, it was proposed that S620 might interact with N629 directly<sup>23,42</sup> or via a water-mediated interaction<sup>23</sup>, analogous to the E71-D80 interaction seen in WT KcsA<sup>10,11,17</sup>. Given the shorter S620 side chain (compared to E71) an interaction between the side chain of S620 and N629 results in a buckling of the selectivity filter in HERG<sup>23,42</sup>. Rather than interaction with S620, our structures show an interaction between the side chains of N629 and Y616 that is preserved in both the high and low-K structures (Fig. 2B) and so could serve to scaffold the upper part of the filter to the pore-helix in both

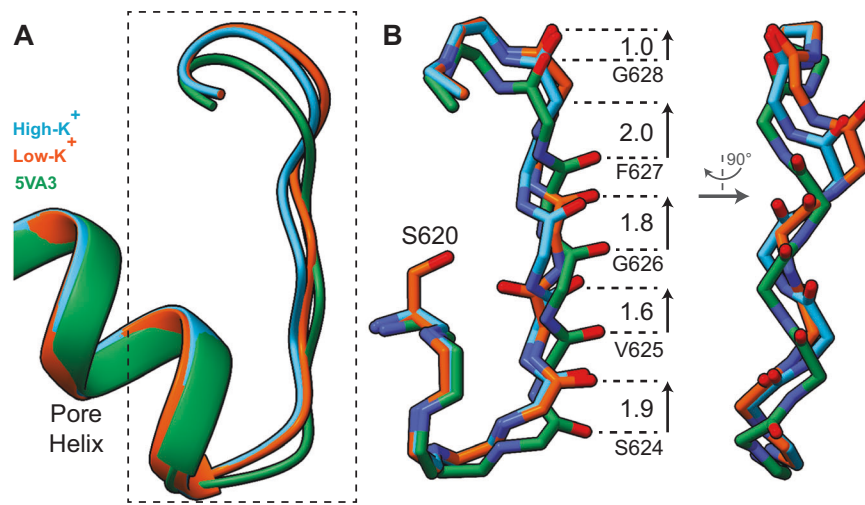


**Fig. 5 | Comparison between selectivity filter structures in WT high-K, WT low-K, and S631A HERG.** **A** The three structures (orange: WT Low-K, blue: WT High-K, green: S631A, 5va3.pdb) were aligned on the pore helix regions. The S631A filter (green) is displaced downwards relative to the WT structures. **B** Highlight of the

boxed region from A, showing the relationship between the backbone atoms in the selectivity filter. Distances on left side indicate vertical displacement of backbone C $\alpha$  atoms for S631A and WT low-K.

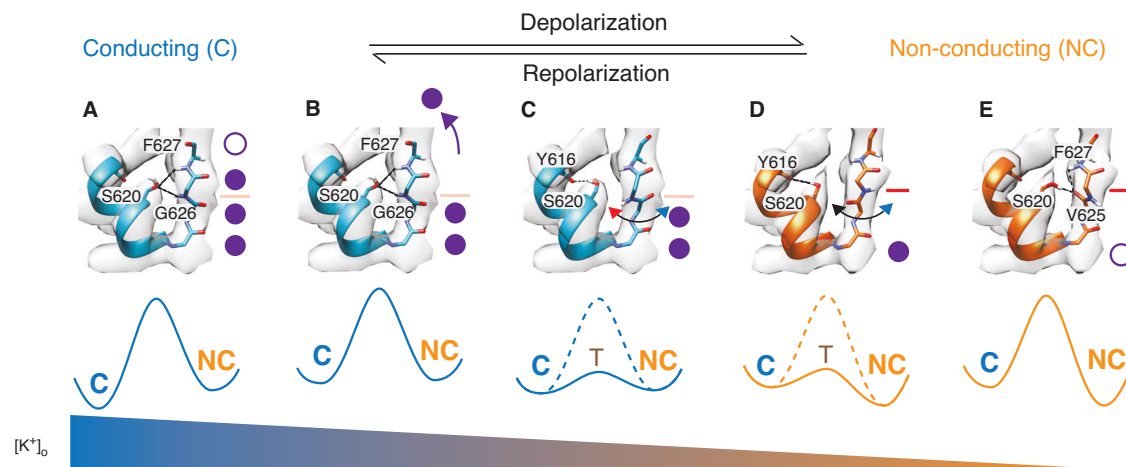


**Fig. 6 | Proposed model for transition from conducting to non-conducting selectivity filter.** Cryo-EM maps of the selectivity filter obtained from the high-K structure (panels A–C) and low-K structure (panels D, E) with superimposed protein structures obtained from snapshots of the MDFF fits to the high-K (blue) or low-K (orange) cryo-EM maps. Stylized free energy diagrams for the transition from the conductive (C) to non-conductive (NC) state, via a transition state (T) are shown below each panel. Interactions stabilizing each state are highlighted as dashed lines in each panel (A, B: S620 – F627/G626, C, D: S620 – Y616; E: S620–V625). The

transition from conducting to non-conducting states is initiated by K<sup>+</sup> ions leaving the upper filter. **B** The energy barrier for movement of ions between S3 and S2 (faint pink line, panels A–C) is increased when all four V625 backbone carbonyls are flipped (red line in panels D, E). The gradient for [K<sup>+</sup>]<sub>o</sub> indicates that the conductive state is favored at high [K<sup>+</sup>]<sub>o</sub> and the non-conducting state is favored at low [K<sup>+</sup>]<sub>o</sub>. A movie depicting the transition from the conductive to non-conductive states is shown in Supplementary Movie 1.

conducting and non-conducting states. Given the tight packing in this area, it is perhaps not surprising that mutations to either N629 or Y616 either produce non-functional channels or have significant changes to function (e.g. N629D channels are non-selective for K<sup>+</sup> over Na<sup>+</sup><sup>43</sup> and Y616L alters both activation and inactivation<sup>38</sup>). Perhaps the most informative mutation is that of Y616F which removes a single hydroxyl side chain. This mutation enhances inactivation which suggests that the interaction between the Y616 and N629 side chains is relatively more important for stabilizing the open state than the inactivated state. We also note that there is an interaction between the homologous residues in KcsA (D80 and W67)<sup>10,11,14</sup> that can be seen in both conducting and non-conducting filters.

Comparison between HERG and the recent structures of Shaker, and the homologous Kv1.3, are more tenuous. In Shaker, the V438 side chain (equivalent to S620 in HERG) cannot form hydrogen bonds and

the putative inactivated state appears to have a distinct structure with dilatation of the upper filter<sup>18–21</sup>. The published structures for the “inactivated” state of Shaker, however, are based on mutant structures, rather than changes in K<sup>+</sup> concentration. In a recent MD simulation study of HERG, Pettini and colleagues showed that mutants that promoted inactivation led to widening of the extracellular entrance of the channel, but less prominent than what was seen in Shaker<sup>25</sup>. In our cryo-EM structures we observed a small dilatation of the upper filter, in both the high-K and low-K structures (Supplementary Fig. S6). Both our data and the MD simulations from Pettini et al.<sup>25</sup> are consistent with the conducting state of the filter being sensitive to loss of K<sup>+</sup> from the extracellular side, which has been shown to represent the first step in the transition from the open to inactivated state<sup>30</sup>.

The other channel for which high-K and low-K structures are available is the heterodimeric K2P.1 (Trek1) channel<sup>12</sup>. These channels

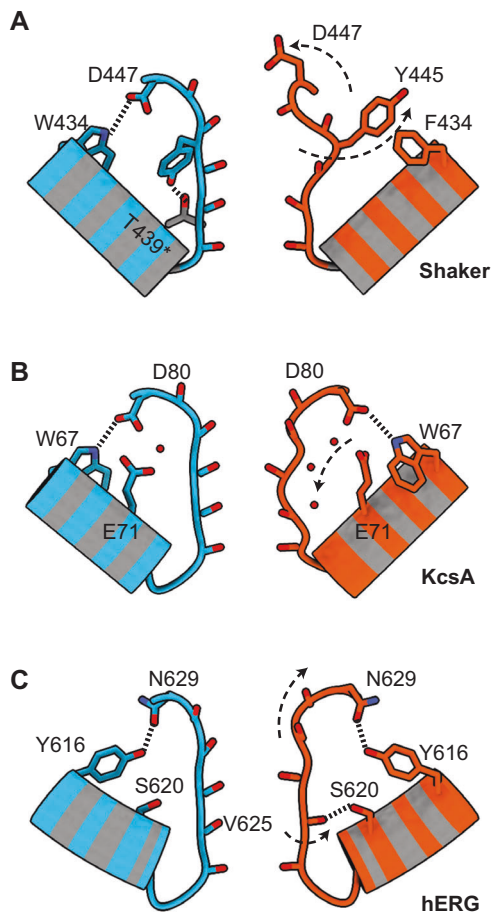


**Fig. 7 | Different channels adopt different non-conducting selectivity filter structures.** Structures of the conducting (blue) and non-conducting (orange) filters for Shaker, KcsA, and hERG. **A** In Shaker channels there is dilatation of the central glycine and tyrosine backbone carbonyls but little change in the lower filter<sup>18,19</sup>. **B** In KcsA, the non-conductive state is characterized by constriction of the central glycine backbone carbonyls, an incomplete rotation of the valine backbone carbonyls away from the central axis<sup>10</sup> and changes in water occupancy<sup>17</sup>. **C** The non-conductive state in hERG is more like KcsA than Shaker but involves a complete rotation of the V625 backbone carbonyls, stabilized by an interaction with the S620 side chain and no change in the number of water molecules.

undergo asymmetric changes with pinching of one of the two selectivity filter sequences but dilatation of the second selectivity filter sequence, further supporting the hypothesis that all  $K^+$  channels adopt a similar conductive conformation, but each adopt different non-conducting filter configurations. It has been suggested that the non-conducting selectivity filter of hERG may involve asymmetric changes<sup>24</sup>. In our MD studies, the flipping of the V625 backbone carbonyls occurred in individual subunits, which resulted in some asymmetric changes. The asymmetry that we observed, however, was small, including in the extensive REST2 simulations which sampled broad-ranging configurations of the selectivity filter (Supplementary Fig. S13). This is consistent with the lack of significant asymmetry in the low-K structure determined by cryo-EM.

Finally, there are some features of hERG inactivation that our model does not yet answer. For example, in the proposed three step mechanism, (i) exit of ions from the extracellular filter, (ii) flipping of the V625 backbone carbonyls, and (iii) stabilization of the flipped V625 backbone carbonyl via its interaction with the S620 side chain (Fig. 6), we cannot determine which of these is the rate determining step. The energy barrier for rotation of individual V625 backbone carbonyls is only 4–5 kcal/mol (Fig. 3C) but from the REST2 simulations we suggest

that at least 3, and possibly all four, V625 backbone carbonyls must be stabilized in the flipped state for the channel to become non-conducting. Furthermore, when a V625 backbone carbonyl initially flips, the S620 side chain will be interacting with the Y616 backbone carbonyl and so the V625 backbone carbonyl is more likely to flip back (-1.8 kcal/mol free energy barrier) than remain flipped by interacting with the S620 side chain (-6 kcal/mol free energy barrier). So, we suggest that flipping per se is not the rate limiting step. We cannot yet determine, however, whether the stabilization of the flipped V625 backbone carbonyl by interaction with S620 side chain or exit of  $K^+$  ions from the extracellular end of the filter represents the rate limiting step. Furthermore, while the REST2 simulations strongly suggest that when all four V625 carbonyls are stabilized in the flipped state, the channel is non-conducting, we cannot rule out the possibility that only three flipped V625 carbonyls may be sufficient to stabilize the non-conducting state. In future studies, it would also be important to consider the impact that using different force fields in MD simulations could have on distribution of ion configurations and their effects on filter structure<sup>32</sup>. Our proposed model also does not address the origin of the voltage-sensitivity of hERG inactivation. Our cryoEM datasets, did not show significant rearrangements in the voltage sensor domain between conducting and non-conducting states (Fig. 1C), consistent with much previous literature showing that mutations to charged residues in the voltage sensor domain have minimal impact on hERG inactivation<sup>44</sup>. The lack of any changes in the orientation of the extracellular SSP domain, between conducting and non-conducting states, was more surprising, given that mutations in the SSP domain have a profound effect on the voltage-sensitivity of hERG inactivation<sup>45</sup>. The changes in the height of the selectivity filter in the S631A mutant channel compared to low-K hERG channels (Fig. 5) could provide a clue to the origin of voltage sensitivity, as these changes could alter the local electric field strength. Investigation of the voltage-sensitivity of hERG inactivation could be facilitated by structural studies of mutant channels with altered voltage sensitivity and/or analysis of channels in lipid vesicles that can be studied in the presence and absence of a voltage gradient as has recently been undertaken for HEAG channels<sup>46</sup>.

In summary, the structure of the conducting filter for hERG resembles that seen for KcsA and Shaker, but the non-conducting filters are all different to each other. These subtle differences can explain the uniquely rapid inactivation kinetics of hERG channels and paves the way for future structural investigations into understanding how clinically occurring mutations in the vicinity of the selectivity filter, as well as movement of the activation gate, alter the distribution between conducting and non-conducting states of hERG.

## Methods

Please refer to Supplementary Table S2 for Key Resources.

## Ethical statement

The Garvan/St Vincent's Animal Ethics Committee approved all experiments (23/11).

## Electrophysiology studies

**Xenopus oocyte recordings.** Oocytes were isolated from *Xenopus laevis* frogs (2–6 years of age; purchased from Nasco, Fort Atkinson, WI, USA). Frogs were anaesthetized in 0.17% w/v tricaine and segments of ovarian lobes were removed through a small abdominal incision. The ovarian lobes were digested with collagenase A (2 mg ml<sup>-1</sup>, Boehringer Mannheim USA) in a buffered salt solution containing (mm): NaCl 82.5, KCl 2.0, MgCl<sub>2</sub> 1.0 and Hepes 5.0 (pH adjusted to 7.5 with NaOH). Oocytes were manually teased apart and rinsed with ND96 containing (mm): KCl 2.0, NaCl 96.0, CaCl<sub>2</sub> 1.8, MgCl<sub>2</sub> 1.0 and Hepes 5.0 (pH adjusted to 7.5 with NaOH). Batches of 100–200 Stage V/VI oocytes were isolated and stored at 16 °C in ND96 containing freshly



prepared Na pyruvate (2.5 mM), theophylline (0.5 mM), and gentamicin (10  $\mu\text{g ml}^{-1}$ )<sup>45</sup>.

WT HERG cDNA was a gift from Gail Robertson (University of Wisconsin). cRNA was synthesized using the Invitrogen™ mMACHINE T7 Transcription Kit (Thermo Fisher Scientific, Riverstone NSW) according to the manufacturers' protocols. Oocytes were injected with 23 nL cRNA and incubated for -24 h prior to electrophysiological recordings, using a Geneclamp-500B amplifier (Molecular Devices, San Jose, CA). All experiments were undertaken at room temperature (21–22 °C). Perfusion solutions contained 3 mM KCl, 97 mM NaCl, 1.8 mM  $\text{CaCl}_2$ , 1 mM  $\text{MgCl}_2$ , 5 mM HEPES, pH adjusted to 7.5 with NaOH. Glass microelectrodes had tip resistances of 0.2–0.7 M $\Omega$  when filled with 3 M KCl. Data analysis was performed using pClamp software (Version 10.6, Molecular Devices) and Excel software (Microsoft Corporation, Seattle, WA). All data are shown as mean  $\pm$  S.E.M.

Steady-state inactivation was measured from a two-step voltage protocol, as previously described<sup>45</sup>. The voltage range for measurement of inactivation in *Xenopus* oocytes extended to -200 mV for mutants with enhanced inactivation and up to +100 mV for mutants with reduced inactivation. For HEK293 cells inactivation was measured over a voltage range from -150 mV to +20 mV. Peak tail currents were obtained by fitting an exponential function to the decay phase of the tail currents and extrapolating back to the start of the voltage step, i.e., to account for channel deactivation<sup>24</sup>. Normalized conductance values were then fitted with a Boltzmann function:

$$g/g_{\max} = [1 + \exp((\Delta G_0 - z_g E F) / RT)]^{-1} \quad (1)$$

where  $\Delta G_0$  is the free energy difference between the open and inactivated states at 0 mV.  $z_g$  is the charge transferred during inactivation,  $E$  is the electric field strength,  $F$  is Faraday's constant,  $R$  is the Universal Gas constant and  $T$  is temperature.

### Protein expression and purification

The cryo-EM construct used for the study of Human KCNH2 (HERG) was based on the Ts construct developed by Wang and Mackinnon<sup>22</sup>. In brief cytoplasmic loops 141–380 and 871–1005 were removed using quikchange PCR methods. A TEV protease site (ENLYFQG) was inserted between the gene and a GFP epitope followed by a double strep tag (AWSHPQFEK) with a linker (GGGS)<sub>2</sub> (GGSAA) between the first and second repeat. The construct was cloned using EcoRI and XbaI into PEG vector<sup>47</sup>.

The PEG-HERG construct was used to generate baculovirus as described in ref. 47. Cells were cultured and purifications were performed with changes as described<sup>22</sup>. Briefly, HEK 293 GnTI- cells were induced with baculovirus when reaching a density of  $2.5\text{--}3.5 \times 10^6$  cells/ml. After 24 h from induction the temperature was lowered to 30 °C and a final concentration of 10 mM sodium butyrate was added for a further 24 h where cells were harvested.

Cells were lysed in 30 mM KCl and 20 mM HEPES pH 7.4 and spun down at 40,000 rpm for 90 min. The insoluble fraction was collected and resuspended in 300 mM KCl, 20 mM HEPES pH 7.4, 1% DDM n-Dodecyl- $\beta$ -D-maltoside (DDM), 0.2% Cholesteryl hemisuccinate (CHS) and 5 mM DTT, samples were incubated at 4 °C for one hour under gently agitation. The soluble fraction was collected and loaded onto strep-tactin superflow high-capacity resin (IBA) and allowed to bind at a flow rate of 1 ml/min at 4 degrees. Resin was washed (300 mM KCl, 20 mM HEPES pH 7.4, 0.1% DDM, 0.02% Cholesteryl hemisuccinate (CHS), 5 mM DTT and 0.1 mg/ml phospholipids POPC, POPE and POPA in a ratio of 5:5:1) with 5 column volumes or until UV absorption returned to baseline. The sample was eluted with an addition of 5 mM Desthiobiotin to the wash buffer. For WT HERG, GPF was cleaved with TEV protease overnight at 4 °C under gentle agitation. The Tetramer peak was collecting using a Superose 6 using either 300 mM KCl or

3 mM KCl and 297 mM NaCl, 20 mM HEPES pH 7.4, 10 mM DTT, 0.025% DDM, 0.005% CHS and 0.025 mg/ml of phospholipids POPC, POPE and POPA in a ratio of 5:5:1. Protein was concentrated to 7.5 mg/ml.

### Cryo-EM grid preparation and data collection

Quantifoil® 200 Cu mesh RL2/1.3 holey Cu-carbon grids were plasma cleaned for 60 s in low pressure gas (0.5 mbar, 80% argon 20% oxygen mixture) using a Diener plasma cleaner. Protein sample (3.5  $\mu\text{l}$ ; 7.5–8.5 mg/ml) was applied to the carbon-coated side of the grid. The grid was blotted for 10 s with blot force 10 and vitrified in liquid ethane using a Vitrobot Mark IV (FEI) equilibrated to 4 °C and 100% humidity.

For all datasets, grids were imaged on a Titan Krios operating at 300 keV equipped with a Gatan K2 detector. Images were collected in electron counting mode at a nominal microscope magnification of 130kx (1.05 Å/pixel) with  $1e^6/\text{A}^2$  per frame with a total dose of 50  $e^6/\text{A}^2$  or 60  $e^6/\text{A}^2$  and nominal defocus range from -0.5 to -2.5  $\mu\text{m}$ .

### Cryo-EM data processing

Data was processed using RELION-3.1.1. Motion correction was done using RELION<sup>48</sup> and defocus values were estimated using CTFIND4<sup>49</sup>. Auto-picking was first performed on a subset of micrographs for each dataset using a Laplacian of Gaussian filter to generate templates for templated-based auto-picking of the whole dataset. Particles were extracted from micrographs with a box size of 300 pixels and binned to 64 pixels for all datasets. The binned particles were subjected to five rounds of 2D classification. Good classes were manually selected and reextracted without binning. An initial model was generated without imposing symmetry. The extracted particles were initially subjected to one round of 3D classification with 6 classes and no symmetry imposed. No asymmetry was observed in the initial model or any of the classes (see Supplementary Fig. S1). Further 3D classification was therefore performed with C4 symmetry imposed and classes which clearly resemble HERG were selected. Final 3D auto-refinement followed by Bayesian polishing and CTF refinement were performed in RELION. Focused refinement using a soft mask covering only the transmembrane region (398–667) was done using the final polished particles. Focused refinement did not improve resolution or provide better quality map and, therefore, the focused refined map was not used.

Post-processing and resolution estimates were performed with a soft mask including only the transmembrane domains. Local resolution was calculated using the local resolution function in Post-processing job of Relion. Pixel size was calibrated against the published structure (EMD-8650) by maximizing the cross-correlation between the two maps. Calibrated pixel size of the final map was 1.05 Å/pixel for all datasets.

### Model building and refinement

Model was built and refined using ISOLDE<sup>50</sup> and PHENIX<sup>51</sup>. The HERG structure (PDB: 5VA1) was used as starting model. Only the transmembrane domains (residues 398–709) were modeled due to the poorer local resolution for the cytoplasmic domains. MolProbity<sup>52</sup> was used to validate the geometries of the refined models. Difference maps were calculated using TEMPy:Diffmap<sup>53</sup>. The WT high-K and WT low-K maps were first low pass filtered to 3.3 Å, then matched by amplitude scaling in resolution shells and the difference map generated as fractional differences with respect to the globally scaled map values. All images were rendered using ChimeraX-1.4<sup>54</sup>. Internal cavity was calculated using HOLLOW<sup>55</sup> with 1.4 Å radius probe and grid spacing of 0.2 Å.

### Molecular dynamics

All systems were built with CHARMM and simulated with NAMD2.13 or NAMD2.14<sup>56</sup>. The CHARMM36 lipid<sup>57</sup> and CHARMM22 protein force fields<sup>58</sup> with CMAP corrections<sup>59</sup> were used with modified  $\text{K}^+$ -backbone

carbonyl interaction parameters (depth 0.102 kcal/mol and position 3.64 Å of minimum) to achieve a small experimental preferential solvation of K<sup>+</sup> in N-methyl-acetamide over water<sup>60</sup>. The NPT ensemble was maintained using the Langevin piston Nose-Hoover method<sup>61,62</sup> for pressure and Langevin dynamics to maintain a temperature of 303 K. Bonds to hydrogen atoms were maintained with the RATTLE algorithm<sup>63</sup> and electrostatic interactions calculated with Particle Mesh Ewald<sup>64</sup> with a grid spacing of 1.0 Å and 6th order B-spline mesh interpolation with a neighbor list distance of 15 Å and a real space cut-off of 12 Å with energy switch distance of 10 Å.

### Molecular dynamics flexible fitting

To best mimic the experimental system for Molecular dynamics flexible fitting (MDFF)<sup>65</sup> simulations, detergent micelles were built around proteins using PDB:5VAL. The optimal size of the micelle was determined by simulating 6 different sizes of a simple pure detergent micelle (n-Dodecyl-B-Maltoside Detergent (DDM)). The number detergent molecules in contact with the protein plateaus at 400–450 molecules, Supp Fig. S5, suggesting that this is a sufficient number of detergent molecules for embedding HERG<sup>66</sup>. WT HERG, N588K\_HERG and N588E\_HERG were embedded in micelles containing 404 molecules, consisting of detergent (DDM (300)), lipid (POPE (20), POPC (20), POPA (4)) and cholesterol derivative (cholesteryl hemisuccinate (60)), and surrounded with explicit TIP3P water molecules<sup>67</sup>. Micelles were surrounded with 110 853 water molecules and either 660 K<sup>+</sup> ions and 600 Cl<sup>-</sup> ions (300 mM KCl) or 70 K<sup>+</sup> ions and 6 Cl<sup>-</sup> ions (3 mM KCl), respectively.

MDFF<sup>65</sup> was used to refine the cryo-EM structures in the presence of a potential energy function based on the cryo-EM density map  $\Phi(\mathbf{r})$ , given by  $U_{EM}(\mathbf{R}) = \sum \omega_j V_{EM}(\mathbf{r}_j)$ , where  $\omega$  is the weight for each atom  $j$ , and

$$V_{EM}(\mathbf{r}) = \begin{cases} \xi \left( 1 - \frac{\Phi(\mathbf{r}) - \Phi_{thr}}{\Phi_{max} - \Phi_{thr}} \right); & \Phi(\mathbf{r}) \geq \Phi_{thr} \\ \xi; & \Phi(\mathbf{r}) < \Phi_{thr} \end{cases} \quad (2)$$

with threshold,  $\Phi_{thr}$ , to remove noise and scaling factor  $\xi$ . Five independent simulations were performed for each map, where  $\xi$  was progressively increased from 0 to 5 kcal/mol over the first 50 ns followed by 50 ns of constant  $\xi = 5$  kcal/mol. For the WT simulations, the RMSD for the backbone atoms of the pore domain helices and the selectivity filter plateaued after 10 ns and 40 ns, respectively. 50 final structures were generated by energy minimizing with 1000 steps of steepest descent every ns with  $\xi = 10$  kcal/mol starting after 50 ns simulation. For N588K and N588E HERG, a final structure was saved from an MDFF simulation to use as the starting point for subsequent K<sup>+</sup> ion permeation US simulations (see below).

### Molecular dynamics simulations of HERG in membranes

**Simulations of HERG with maintained ion configurations.** MD simulations were performed starting with the WT HERG high-K structure (pdb: 9CHP). The pore domain (residues 545 to 667) was embedded in a lipid bilayer consisting of palmitoyloleoyl-phosphatidylcholine (POPC) lipids (238 molecules). It was surrounded with 18,771 explicit TIP3P water molecules<sup>67</sup> and 150 mM KCl (49 K<sup>+</sup> ions and 53 Cl<sup>-</sup> ions). During initial equilibration, all heavy atoms in the protein, as well as ions in the selectivity filter, were constrained with harmonic constraints with force constants of 10 kcal/mol/Å<sup>2</sup>. Constraints on the protein were slowly released during 5 ns simulations before production runs.

Libraries of 10 independent simulations each of 50 ns were performed for the WT channel with each of 9 different ion configurations in the selectivity filter. Multi-ion configurations in sites S0/S2/S4, S2/S4, and S1/S3 as well as single ion configurations in sites S0–S4 and an empty filter were constrained with flat-bottomed potentials ( $k = 10$  kcal/mol/Å<sup>2</sup> and thickness 3.5 Å) holding the ions in

their sites. Means and distributions were calculated after excluding the first 10 ns of equilibration. Errors bars were calculated as the standard error of means for the 10 different simulations for each ion configuration.

The angle of the selectivity filter backbone carbonyls,  $\theta$ , were calculated as the angle between the projection on the  $xy$ -plane of the vector between the backbone carbonyl C and the backbone carbonyl O and the projection on the  $xy$ -plane of the vector between the backbone carbonyl C and the center of mass of the selectivity filter. Distributions of backbone carbonyl angles (0° indicates pointing towards center of pore) have been plotted as violin plots, and the proportion of time 0, 1, 2, 3, or 4 backbone carbonyls were pointing inwards (defined as <70° deviation from 0°) reported.

Cluster analysis was performed with k-means algorithm<sup>68</sup> in MATLAB using  $k = 10$  clusters and clustering on the backbone  $\Phi$  and  $\Psi$  angles of the selectivity filter (residue 624 to 628). Initial cluster centroids were generated using the k-means++ algorithm. Each point in space was then allocated to its nearest cluster and the cluster centroid recalculated. This was done iteratively until self-consistent. Each subunit was clustered separately to allow for asymmetries. Analysis of backbone carbonyl angles and interaction distances ( $d$ ) was performed based on which cluster the system was in (blue conducting, orange non-conducting). Free energy maps, as function of S620 side chain interactions with V625 backbone carbonyl, G626 amide, F627 amide or Y616 backbone carbonyl plotted against rotation of the V625 backbone carbonyl have been obtained from analysis of all frames of the constrained ion MD simulations of HERG in the membrane. Maps were created from calculation of  $\Delta G(d, \theta) = -k_B T \ln \rho(d, \theta) + C$ , where  $\rho$  is the probability distribution as a function of the interaction distance  $d$  and V625 backbone carbonyl orientation  $\theta$ .

**Conduction simulations.** Simulations starting with either the high-K structure (pdb: 9CHP) or low-K structure (pdb: 9CHQ) were similar to those described above, but included 500 mM KCl solution (165 K<sup>+</sup>, 169 Cl<sup>-</sup> ions and 18,653 water molecules), including 5 K<sup>+</sup> ions that were initially placed at the centers of sites S0–S4 in the equilibrated structure. The CHARMM36 force field without modifications was used for these simulations. This system was run for 0.5  $\mu$ s (two independent simulations) with a constant electric field equivalent to an applied membrane potential of -500 mV (negative inside) to attempt to observe conduction. During equilibration, heavy atom harmonic position restraints on the selectivity filter and resident ions were applied with a force constant of 5 kcal/mol/Å<sup>2</sup>, relaxed to zero slowly over 10 ns. Conduction events were counted after excluding the first 10 ns of equilibration.

To maintain this high-K cryo-EM-like structure, flat-bottom restraints were applied to loosely maintain H bonds identified in the cryo-EM structure. This required a weak flat-bottom restraint (force constant 5 kcal/mol/Å<sup>2</sup> applied when 3.2 Å was exceeded) acting on the distance between the S620 side chain hydroxyl O, and both the G626 and F627 backbone amide H atoms for each subunit, for the conducting structure. This restraint is designed to not be felt unless the H-bond is attempting to break, as would occur during a structural isomerization of the backbone linkage. In addition, a flat-bottom harmonic restraint was applied to the intracellular gate. Specifically, the 6 C $\alpha$ -C $\alpha$  distances connecting adjacent carbon atoms of the same residue were weakly restrained with flat-bottom distance restraints, for the four C $\alpha$  atoms (each) in residues F656, G657, and N658. The 18 flat-bottom restraints had a force constant of 5 kcal/mol/Å<sup>2</sup>, with no force applied until the C $\alpha$  distance deviated more than  $\pm 2$  Å from the distances observed in the experimental structure. These distance restraints were applied to maintain an open gate at the narrowest point.

Two identical simulations were also run starting with the low-K structure for 0.5  $\mu$ s each. In this case, an equivalent constraint was

applied to maintain the identified H bond between the S620 hydroxyl H atom and the flipped backbone carbonyl O atom of residue V625.

**Umbrella sampling simulations of the V625 backbone carbonyl.** Umbrella sampling simulations<sup>69</sup> of the rotation of the V625 backbone carbonyl was performed by constraining the V625 backbone  $\Psi$  angle (N<sub>625</sub>-C<sub>625</sub>-C<sub>α625</sub>-N<sub>626</sub>). The backbone  $\Psi$  angle controls the V625-Gly626 linkage and thus the orientation of the V625 backbone carbonyl oxygen (with  $\Psi \sim -50^\circ$  leading to the backbone carbonyl oxygen pointing in and  $\Psi \sim +70^\circ$  leading to the backbone carbonyl oxygen pointing out). This backbone dynamics has previously been shown in both KcsA and MthK<sup>15,29</sup>. Initial windows were created using steered MD with a harmonic force constant of 0.03 kcal/mol/Å<sup>2</sup> moving at a rate of 0.2 ns/°. The complete 360°  $\Psi$  rotation was divided into 72 windows separated by 5°. The backbone dihedral was constrained with a force constant of 0.03 kcal/mol/Å<sup>2</sup> in the center of each window. During the production run, multi-ions configurations in sites S0/S2/S4, S2/S4, S2/S3, and S1/S3 were constrained in their sites with flat-bottom potentials ( $k = 10$  kcal/mol/Å<sup>2</sup> and width 3.5 Å). Simulations were performed for the WT channel with ions in S0/S2/S4, S1/S3. A convergence criterion of a free energy change of less than 1 kcal/mol was used and this was achieved after 9 ns and 11 ns for WT with ions in S0/S2/S4 or S1/S3. All data prior to equilibration was discarded for final calculations. WHAM<sup>70</sup> with periodic boundary conditions was used to calculate the free energy profile. Error bars were calculated as standard error of mean by dividing the data into 1 ns long blocks.

**Replica exchange with solute tempering.** To study the behavior of the filter at 300 K temperature, replica exchange with solute tempering (REST2) simulations<sup>31</sup> starting with the conductive structure were performed. 3 K<sup>+</sup> ions were trapped in the vicinity of the selectivity filter/cavity region using a tall cylinder of 30 Å height and 15 Å width with flat-bottom half-harmonic constraints of 10 kcal/mol/Å<sup>2</sup>. Sixteen replicas with effective temperatures for ion interactions from 300 K to 900 K were used, where only the interactions involving the 3 trapped ions were scaled. Two independent systems, with ions starting in S0/S2/S4, or with S1/S3/cavity, were simulated for 500 ns each. The free energy profile,  $\Delta G(z) = -k_B T \ln \rho(z) + C$ , using only trajectory from the individual replicas of both simulations, is shown in Fig. S9 to demonstrate reproducibility across replicas and convergence over time. Here,  $\rho$  is the probability distribution as a function of reaction coordinate  $z$ , where  $z$  is the position of an ion along the  $z$  coordinate with respect to the center of mass of the backbone atoms of the selectivity filter. The constant,  $C$ , was chosen to set the free energy to zero in the extracellular solution. This effective free energy profile based on ion density due to the 3 ions trapped in the channel, reveals the apparent locations and depths of the binding sites, as well as the apparent barriers for ion movement between sites, but is distinct from the barriers that would be seen in a multi-ion permeation mechanism. It is thus used as a guide to understand the propensities for ion binding and movement.

**MBAR free energy analysis of REST2 simulations.** We have used MBAR<sup>33</sup> to make full use of the sampling obtained in all 16 replicas of the two independent REST2 simulations. MBAR has been used for capturing the barriers in the 1D ion free energy profile in cases with 0–4 flipped V625 backbone carbonyls (Fig. 3D), and to improve sampling of barriers in 2D maps for S620 interactions (Fig. 4C–F). Our approach is based on the publicly available pyMBAR code for replica exchange<sup>33</sup>, modified to use ion interaction energies from REST2 with our own in-house codes. We sampled from trajectory infrequently (every 20 ps), to ensure uncorrelated samples.

Analysis for the free energy of ions inside the selectivity filter (Fig. 3D) was performed by analyzing  $z$  position of each trapped ion (grid size 0.4 Å), together with the number of flipped V625 backbone carbonyls, to form 2-dimensional histograms. Individual PMFs for

different number of flipped carbonyls were obtained by extracting cross-sections from the 2D map for each individual number of flipped carbonyls to produce separate 1D PMFs. The number of carbonyls that were pointing towards the channel axis was defined by testing whether the  $\Psi$  dihedral angle exceeded a cutoff of +30°, based on the flipping barriers seen in Fig. 3C; with the value chosen to ensure the barrier is overcome regardless of the ion configuration. Error bars in 1D free energy profiles represent  $\pm$  one standard deviation obtained from MBAR<sup>33</sup>.

Free energy maps for S620 side chain hydrogen-bonding interactions with surrounding residues (Fig. 4C–F) were also analyzed using MBAR. Two-dimensional histograms were formed as a function of the carbonyl angle away from the channel axis ( $\theta$ ; defined above; grid size 10°) and a distance involving the S620 side chain. The distances analyzed included that between S620 side chain hydroxyl H and V625 backbone carbonyl O or Y616 backbone carbonyl O, as well as S620 side chain hydroxyl O with V626 backbone amide H or F627 backbone amide H (bin size 0.2 Å). Errors in barrier estimates were obtained from MBAR errors at the location of highest free energy along the minimal free energy pathway between two states.

### Reporting summary

Further information on research design is available in the Nature Portfolio Reporting Summary linked to this article.

### Data availability

The data that support this study are available from the corresponding authors upon request. The cryo-EM maps have been deposited in the Electron Microscopy Data Bank (EMDB) under accession codes **EMDB-45597** (High-K<sup>+</sup>; C4); **EMDB-45598** (Low-K<sup>+</sup>; C4); **EMDB-45599** (High-K<sup>+</sup>; C1); and **EMDB-45600** (Low-K<sup>+</sup>; C1). The atomic coordinates have been deposited in the Protein Data Bank (PDB) under accession codes **9CHP** (High-K<sup>+</sup>; C4); **9CHQ** (Low-K<sup>+</sup>; C4); **9CHR** (High-K<sup>+</sup>; C1); and **9CHS** (Low-K<sup>+</sup>; C1). Previously published PDB used in this study: **5VA1**; and **5VA3**. The source data underlying Fig. 2D, E are provided as a Source data file. Source data are provided with this paper.

### References

1. Yellen, G. The voltage-gated potassium channels and their relatives. *Nature* **419**, 35–42 (2002).
2. Smith, P. L., Baukrowitz, T. & Yellen, G. The inward rectification mechanism of the HERG cardiac potassium channel. *Nature* **379**, 833–836 (1996).
3. Lu, Y. et al. Effects of premature stimulation on HERG K(+) channels. *J. Physiol.* **537**, 843–851 (2001).
4. Vandenberg, J. I. et al. hERG K(+) channels: structure, function, and clinical significance. *Physiol. Rev.* **92**, 1393–1478 (2012).
5. Osadchii, O. E. Mechanisms of hypokalemia-induced ventricular arrhythmogenicity. *Fundam. Clin. Pharm.* **24**, 547–559 (2010).
6. Huang, F. D., Chen, J., Lin, M., Keating, M. T. & Sanguinetti, M. C. Long-QT syndrome-associated missense mutations in the pore helix of the HERG potassium channel. *Circulation* **104**, 1071–1075 (2001).
7. Zhao, J. T. et al. Not all hERG pore domain mutations have a severe phenotype: G584S has an inactivation gating defect with mild phenotype compared to G572S, which has a dominant negative trafficking defect and a severe phenotype. *J. Cardiovasc. Electrophysiol.* **20**, 923–930 (2009).
8. Ficker, E., Jarolimek, W., Kiehn, J., Baumann, A. & Brown, A. M. Molecular determinants of dofetilide block of HERG K+ channels. *Circ. Res* **82**, 386–395 (1998).
9. Herzberg, I. M., Trudeau, M. C. & Robertson, G. A. Transfer of rapid inactivation and sensitivity to the class III antiarrhythmic drug E-4031 from HERG to M-eag channels. *J. Physiol.* **511**, 3–14 (1998).

10. Zhou, Y., Morais-Cabral, J. H., Kaufman, A. & MacKinnon, R. Chemistry of ion coordination and hydration revealed by a K<sup>+</sup> channel-Fab complex at 2.0 Å resolution. *Nature* **414**, 43–48 (2001).
11. Cheng, W. W., McCoy, J. G., Thompson, A. N., Nichols, C. G. & Nimigean, C. M. Mechanism for selectivity-inactivation coupling in KcsA potassium channels. *Proc. Natl Acad. Sci. USA* **108**, 5272–5277 (2011).
12. Lolicato, M. et al. K(2P) channel C-type gating involves asymmetric selectivity filter order-disorder transitions. *Sci. Adv.* **6**, eabc9174 (2020).
13. Doyle, D. A. et al. The structure of the potassium channel: molecular basis of K<sup>+</sup> conduction and selectivity. *Science* **280**, 69–77 (1998).
14. Cuello, L. G., Jogini, V., Cortes, D. M. & Perozo, E. Structural mechanism of C-type inactivation in K(+) channels. *Nature* **466**, 203–208 (2010).
15. Berneche, S. & Roux, B. A gate in the selectivity filter of potassium channels. *Structure* **13**, 591–600 (2005).
16. Li, J., Ostmeyer, J., Cuello, L. G., Perozo, E. & Roux, B. Rapid constriction of the selectivity filter underlies C-type inactivation in the KcsA potassium channel. *J. Gen. Physiol.* **150**, 1408–1420 (2018).
17. Ostmeyer, J., Chakrapani, S., Pan, A. C., Perozo, E. & Roux, B. Recovery from slow inactivation in K<sup>+</sup> channels is controlled by water molecules. *Nature* **501**, 121–124 (2013).
18. Tan, X. F. et al. Structure of the Shaker Kv channel and mechanism of slow C-type inactivation. *Sci. Adv.* **8**, eabm7814 (2022).
19. Reddi, R., Matulef, K., Riederer, E. A., Whorton, M. R. & Valiyaveetil, F. I. Structural basis for C-type inactivation in a Shaker family voltage-gated K(+) channel. *Sci. Adv.* **8**, eabm8804 (2022).
20. Wu, X., Gupta, K. & Swartz, K. J. Mutations within the selectivity filter reveal that Kv1 channels have distinct propensities to slow inactivate. *J. Gen. Physiol.* **154**, e202213222 (2022).
21. Coonen, L. et al. The nonconducting W434F mutant adopts upon membrane depolarization an inactivated-like state that differs from wild-type Shaker-IR potassium channels. *Sci. Adv.* **8**, eabn1731 (2022).
22. Wang, W. & MacKinnon, R. Cryo-EM structure of the open human ether-a-go-go-related K(+) channel hERG. *Cell* **169**, 422–430 e410 (2017).
23. Miranda, W. E. et al. Selectivity filter modalities and rapid inactivation of the hERG1 channel. *Proc. Natl Acad. Sci. USA* **117**, 2795–2804 (2020).
24. Li, J., Shen, R., Reddy, B., Perozo, E. & Roux, B. Mechanism of C-type inactivation in the hERG potassium channel. *Sci. Adv.* **7**, eabd6203 (2021).
25. Pettini, F., Domene, C. & Furini, S. Early steps in C-type inactivation of the hERG potassium channel. *J. Chem. Inf. Model* **63**, 251–258 (2023).
26. Vandenberg, J. I., Perozo, E. & Allen, T. W. Towards a structural view of drug binding to hERG K(+) channels. *Trends Pharm. Sci.* **38**, 899–907 (2017).
27. Butler, A., Helliwell, M. V., Zhang, Y., Hancox, J. C. & Dempsey, C. E. An update on the structure of hERG. *Front Pharm.* **10**, 1572 (2019).
28. Asai, T. et al. Cryo-EM structure of K(+) bound hERG channel complexed with the blocker astemizole. *Structure* **29**, 203–212 e204 (2021).
29. Boiteux, C., Posson, D. J., Allen, T. W. & Nimigean, C. M. Selectivity filter ion binding affinity determines inactivation in a potassium channel. *Proc. Natl Acad. Sci. USA* **117**, 29968–29978 (2020).
30. Wang, D. T., Hill, A. P., Mann, S. A., Tan, P. S. & Vandenberg, J. I. Mapping the sequence of conformational changes underlying selectivity filter gating in the K(v)11.1 potassium channel. *Nat. Struct. Mol. Biol.* **18**, 35–41 (2011).
31. Wang, L., Friesner, R. A. & Berne, B. J. Replica exchange with solute scaling: a more efficient version of replica exchange with solute tempering (REST2). *J. Phys. Chem. B* **115**, 9431–9438 (2011).
32. Furini, S. & Domene, C. Critical assessment of common force fields for molecular dynamics simulations of potassium channels. *J. Chem. Theory Comput* **16**, 7148–7159 (2020).
33. Shirts, M. R. & Chodera, J. D. Statistically optimal analysis of samples from multiple equilibrium states. *J. Chem. Phys.* **129**, 124105 (2008).
34. Schonherr, R. & Heinemann, S. H. Molecular determinants for activation and inactivation of HERG, a human inward rectifier potassium channel. *J. Physiol.* **3**, 635–642 (1996).
35. Perry, M. D., Ng, C. A. & Vandenberg, J. I. Pore helices play a dynamic role as integrators of domain motion during Kv11.1 channel inactivation gating. *J. Biol. Chem.* **288**, 11482–11491 (2013).
36. Gang, H. & Zhang, S. Na<sup>+</sup> permeation and block of hERG potassium channels. *J. Gen. Physiol.* **128**, 55–71 (2006).
37. Teng, G. et al. Prolonged repolarization and triggered activity induced by adenoviral expression of HERG N629D in cardiomyocytes derived from stem cells. *Cardiovasc Res.* **61**, 268–277 (2004).
38. Bassetto, C. A. Z. Jr., Costa, F., Guardiani, C., Bezanilla, F. & Giacomello, A. Noncanonical electromechanical coupling paths in cardiac hERG potassium channel. *Nat. Commun.* **14**, 1110 (2023).
39. Yellen, G. Keeping K<sup>+</sup> completely comfortable. *Nat. Struct. Biol.* **8**, 1011–1013 (2001).
40. Jekhmane, S. et al. Shifts in the selectivity filter dynamics cause modal gating in K(+) channels. *Nat. Commun.* **10**, 123 (2019).
41. Chakrapani, S. et al. On the structural basis of modal gating behavior in K(+) channels. *Nat. Struct. Mol. Biol.* **18**, 67–74 (2011).
42. Kopfer, D. A. et al. A molecular switch driving inactivation in the cardiac K<sup>+</sup> channel HERG. *PLoS ONE* **7**, e41023 (2012).
43. Lees-Miller, J. P., Duan, Y., Teng, G. Q., Thorstad, K. & Duff, H. J. Novel gain-of-function mechanism in K(+) channel-related long-QT syndrome: altered gating and selectivity in the HERG1 N629D mutant. *Circ. Res.* **86**, 507–513 (2000).
44. Zhang, M., Liu, J. & Tseng, G. N. Gating charges in the activation and inactivation processes of the HERG channel. *J. Gen. Physiol.* **124**, 703–718 (2004).
45. Clarke, C. E. et al. Effect of S5P alpha-helix charge mutants on inactivation of hERG K<sup>+</sup> channels. *J. Physiol.* **573**, 291–304 (2006).
46. Mandala, V. S. & MacKinnon, R. Voltage-sensor movements in the Eag Kv channel under an applied electric field. *Proc. Natl Acad. Sci. USA* **119**, e2214151119 (2022).
47. Goehring, A. et al. Screening and large-scale expression of membrane proteins in mammalian cells for structural studies. *Nat. Protoc.* **9**, 2574–2585 (2014).
48. Zivanov, J. et al. New tools for automated high-resolution cryo-EM structure determination in RELION-3. *Elife* **7**, e42166 (2018).
49. Rohou, A. & Grigorieff, N. CTFIND4: fast and accurate defocus estimation from electron micrographs. *J. Struct. Biol.* **192**, 216–221 (2015).
50. Croll, T. I. ISOLDE: a physically realistic environment for model building into low-resolution electron-density maps. *Acta Crystallogr D. Struct. Biol.* **74**, 519–530 (2018).
51. Liebschner, D. et al. Macromolecular structure determination using X-rays, neutrons and electrons: recent developments in Phenix. *Acta Crystallogr D. Struct. Biol.* **75**, 861–877 (2019).
52. Williams, C. J. et al. MolProbity: more and better reference data for improved all-atom structure validation. *Protein Sci.* **27**, 293–315 (2018).
53. Joseph, A. P. et al. Comparing cryo-EM reconstructions and validating atomic model fit using difference maps. *J. Chem. Inf. Model* **60**, 2552–2560 (2020).
54. Pettersen, E. F. et al. UCSF ChimeraX: structure visualization for researchers, educators, and developers. *Protein Sci.* **30**, 70–82 (2021).
55. Ho, B. K. & Gruswitz, F. HOLLOW: generating accurate representations of channel and interior surfaces in molecular structures. *BMC Struct. Biol.* **8**, 49 (2008).

56. Phillips, J. C. et al. Scalable molecular dynamics with NAMD. *J. Comput. Chem.* **26**, 1781–1802 (2005).
57. Klauda, J. B. et al. Update of the CHARMM all-atom additive force field for lipids: validation on six lipid types. *J. Phys. Chem. B* **114**, 7830–7843 (2010).
58. MacKerell, A. D. et al. All-atom empirical potential for molecular modeling and dynamics studies of proteins. *J. Phys. Chem. B* **102**, 3586–3616 (1998).
59. Mackerell, A. D. Jr, Feig, M. & Brooks, C. L. 3rd Extending the treatment of backbone energetics in protein force fields: limitations of gas-phase quantum mechanics in reproducing protein conformational distributions in molecular dynamics simulations. *J. Comput. Chem.* **25**, 1400–1415 (2004).
60. Noskov, S. Y., Berneche, S. & Roux, B. Control of ion selectivity in potassium channels by electrostatic and dynamic properties of carbonyl ligands. *Nature* **431**, 830–834 (2004).
61. Feller, S. E., Zhang, Y. H., Pastor, R. W. & Brooks, B. R. Constant-pressure molecular-dynamics simulation—the Langevin piston method. *J. Chem. Phys.* **103**, 4613–4621 (1995).
62. Martyna, G. J. Remarks on “Constant-temperature molecular dynamics with momentum conservation”. *Phys. Rev. E Stat. Phys. Plasmas Fluids Relat. Interdiscip. Top.* **50**, 3234–3236 (1994).
63. Andersen, H. C. Rattle—a velocity version of the shake algorithm for molecular-dynamics calculations. *J. Comput. Phys.* **52**, 24–34 (1983).
64. Darden, T., York, D. & Pedersen, L. Particle mesh Ewald—an N.Log(N) method for Ewald sums in large systems. *J. Chem. Phys.* **98**, 10089–10092 (1993).
65. Trabuco, L. G., Villa, E., Mitra, K., Frank, J. & Schulten, K. Flexible fitting of atomic structures into electron microscopy maps using molecular dynamics. *Structure* **16**, 673–683 (2008).
66. Cheng, X., Kim, J. K., Kim, Y., Bowie, J. U. & Im, W. Molecular dynamics simulation strategies for protein-micelle complexes. *Biochim Biophys. Acta* **1858**, 1566–1572 (2016).
67. Jorgensen, W. L., Chandrasekhar, J., Madura, J. D., Impey, R. W. & Klein, M. L. Comparison of simple potential functions for simulating liquid water. *J. Chem. Phys.* **79**, 926–935 (1983).
68. MacQueen, J. In *Proceedings of the Fifth Berkeley Symposium on Mathematical Statistics and Probability* 281–297 (Oakland, 1967).
69. Torrie, G. M. & Valleau, J. P. Non-physical sampling distributions in monte-carlo free-energy estimation—umbrella sampling. *J. Comput. Phys.* **23**, 187–199 (1977).
70. Kumar, S., Bouzida, D., Swendsen, R. H., Kollman, P. A. & Rosenberg, J. M. The weighted histogram analysis method for free-energy calculations on biomolecules. 1. The method. *J. Comput. Chem.* **13**, 1011–1021 (1992).

## Acknowledgements

We thank JingTing Zhao and members of the Hill and Vandenberg labs, Michael Clark and members of the Perozo Lab, and Celine Boiteux and members of the Allen Lab for assistance and advice during the project. We thank Terry Campbell, Bob Graham, Richard Harvey, Dan Roden, Benoit Roux, and Mike Sanguinetti for comments on the manuscript. This work was funded in by Australian Research Council Grants DP150101929 (J.I.V.), DP170101732 (T.W.A.), DP200102540 (J.I.V. and E.P.), DP210102405 (T.W.A.), DP220103550 (T.W.A.), National Health and Medical Research Council Grants APP1116948 (J.I.V.), APP1141974 (J.I.V., T.W.A., A.G.S., and E.P.), National Institutes of Health Grant 1R01GM150272 (E.P. and J.I.V.), National Computational Initiative dd7

(T.W.A.). We also wish to acknowledge the Victor Chang Cardiac Research Institute Innovation Centre, funded by the NSW Government, and the Electron Microscope Unit at UNSW Sydney, funded in part by the NSW Government. T.W.A., K.M.C., B.W.N., and E.F. acknowledge support from the Medical Advances Without Animals Trust and A.G.S. acknowledges support from the Australian Research Council Industrial Transformation Training Centre for Cryo-Electron Microscopy of Membrane Proteins for Drug Discovery (IC200100052).

## Author contributions

J.I.V., T.W.A., and E.P. designed and conceived the study. C.L., M.J.H., and J.I.V. designed and performed biochemistry experiments. C.L., M.J.H., A.G.S., J.B., E.P., and J.I.V. designed and performed cryo-EM experiments; C.L., M.J.H., A.G.S., E.P., and J.I.V. analyzed cryo-EM datasets. T.W.A., E.F., and J.I.V. designed the simulation experiments; E.F., K.M.C., B.W.N., and T.W.A. performed and analyzed the simulations. M.J.H., C.-A.N., and J.I.V. designed and performed electrophysiology experiments. The manuscript was written by C.L., E.F., M.J.H., E.P., T.W.A., and J.I.V. with input from all authors.

## Competing interests

The authors declare no competing interests.

## Additional information

**Supplementary information** The online version contains supplementary material available at <https://doi.org/10.1038/s41467-024-51208-w>.

**Correspondence** and requests for materials should be addressed to Toby W. Allen or Jamie I. Vandenberg.

**Peer review information** *Nature Communications* thanks Simone Furini, Toshio Moriya, and the other, anonymous, reviewers for their contribution to the peer review of this work. A peer review file is available.

**Reprints and permissions information** is available at <http://www.nature.com/reprints>

**Publisher's note** Springer Nature remains neutral with regard to jurisdictional claims in published maps and institutional affiliations.

**Open Access** This article is licensed under a Creative Commons Attribution-NonCommercial-NoDerivatives 4.0 International License, which permits any non-commercial use, sharing, distribution and reproduction in any medium or format, as long as you give appropriate credit to the original author(s) and the source, provide a link to the Creative Commons licence, and indicate if you modified the licensed material. You do not have permission under this licence to share adapted material derived from this article or parts of it. The images or other third party material in this article are included in the article's Creative Commons licence, unless indicated otherwise in a credit line to the material. If material is not included in the article's Creative Commons licence and your intended use is not permitted by statutory regulation or exceeds the permitted use, you will need to obtain permission directly from the copyright holder. To view a copy of this licence, visit <http://creativecommons.org/licenses/by-nc-nd/4.0/>.

© The Author(s) 2024